The Aeronautical Journal (2024), 1–16
doi:10.1017/aer.2024.64

ROYAL AERONAUTICAL SOCIETY

RESEARCH ARTICLE

Model compensation control of composite vertical take-off and landing UAV

G.Y. Qi[1], X.R. Zhang[1] and L. Xu[2]

[1]School of Control Science and Engineering, Tiangong University, Tianjin, China
[2]School of Mechanical Engineering, Tiangong University, Tianjin, China
Corresponding author: G.Y. Qi; Email: guoyuanqisa@qq.com

Received: 16 April 2024; **Revised:** 1 June 2024; **Accepted:** 4 June 2024

Keywords: Composite vertical take-off and landing; compensation function observer; model compensated control

Abstract

The unmanned aerial vehicle (UAV) system for composite vertical take-off and landing (VTOL) is a complex, highly coupled, and nonlinear system which is sensitive to external disturbances and model uncertainties. The composite VTOL UAV system consists of a multi-rotor section and a fixed-wing section. To improve observation accuracy, the compensation function observer (CFO) uses a new structure that includes velocity information. The CFO is utilised to estimate the uncertainty and the external disturbances of the system model, which performs superior estimation accuracy compared to the extended state observer (ESO). In the modeling process of the VTOL UAV, the aerodynamic moment is calculated by means of the cross-product operation of force and force arm, which solves the problem of over-reliance on aerodynamic parameters in the traditional modeling approach. The controlled object is refined by CFO, and model compensation control (MCC) is used to realise the velocity and attitude control of the composite VTOL. The numerical simulation of MATLAB/Simulink and hardware-in-loop simulation (HIL) of Rflysim were implemented, and which were used to compare the MCC, active disturbance rejection control (ADRC), and proportion integration differentiation (PID). The simulation results confirm the superiority of MCC in controlling composite VTOL UAVs in terms of anti-disturbance and tracking speed.

Nomenclature

cla, cda	lift and drag parameters in fixed-wing mode
C_{de}, C_{le}	drag and lift coefficient of the elevator
d_{mc_i}	model uncertainty and unknown disturbances of the UAV in multi-rotor mode
d_{fw_i}	model uncertainty and unknown disturbances of the UAV in fixed-wing mode
D	drag applied to the UAV in fixed-wing mode
F	tensile force exerted on the UAV in multi-rotor mode
g	gravitational acceleration
I_x, I_y, I_z	three-axis rotational moment of inertia of the UAV
l	half-wheelbase of the UAV
L_e, D_e	lift force and drag force on the elevator
m	quality of the UAV
M_{ia1}, M_{ia2}, M_{ie}	aerodynamic moments generated by the left aileron, right ailero, and elevator in fixed-wing mode
M_p, M_q, M_r	combined moment applied to each channel in the airflow coordinate system in fixed-wing mode
M_{peD}, M_{qeD}, M_{reD}	three-axis aerodynamic moment generated by the DRAG force acting on the elevator in fixed-wing mode
M_{peL}, M_{qeL}, M_{reL}	three-axis aerodynamic moment generated by the lift force acting on the elevator in fixed-wing mode
M_{pn}, M_{qn}, M_{rn}	three-axis aerodynamic moment of each rudder surface in fixed-wing mode

M_{Ti}	thrust moment applied to each channel in fixed-wing mode
M_{wi}	aerodynamic moment applied to each channel in fixed-wing mode
p, q, r	angular velocity of the UAV in the body coordinate system
Q	dynamic pressure
S_{a1}, S_e	area of left aileron and elevator
T	thrust applied to the UAV in fixed-wing mode
u, v, w	velocity of the UAV in the body coordinate system
x_{a1}, y_{a1}, z_{a1}	position of the force centre of the left aileron relative to the centre of gravity of the UAV
x_e, y_e, z_e	position of the force centre of the elevator relative to the centre of gravity of the UAV

Greek symbol

α	attack angle of the UAV
β	sideslip angle of the UAV
δ_{a1}, δ_{a2}, δ_e	deflection of left aileron, right aileronthe and elevator
ϕ, θ, ψ	roll angle, pitch angle, and yaw angle of the UAV
τ_p, τ_q, τ_r	torque of the attitude angular channel

1.0 Introduction

The use of unmanned aerial vehicle (UAV) has become increasingly widespread in both military and civilian applications due to the continuous development of UAV technology. Fixed-wing UAV has longer endurance, better load capacity and wider operating space than multi-rotor UAV due to their unique structure [1]. However, their work scenarios are limited due to the need for longer runways for takeoff. To overcome these difficulties, vertical take-off and landing (VTOL) UAV has gained more attention. The VTOL UAV combines the advantages of both fixed-wing and multi-rotor UAV. It does not require a runway for vertical take-off and landing manoeuvers. The ability to switch between the two modes allows it to hover at specific locations for high-altitude operations, making it more convenient for tasks such as photo-taking and recording. Common types of VTOL UAVs include tilt-wing, tail-sitter, and composite models [2, 3]. The composite VTOL UAV is chosen as the research object due to its stability in flight mode switching, simpler design and more flexible control algorithm building compared to other options.

Composite VTOL UAVs use two main classes of control algorithms: model-independent and model-dependent. Model-independent algorithms, such as PID control algorithm [4], high order differential feedback control algorithm (HODFC) [5] and total energy control (TECS) [6] are simple to design but cannot adapt to new data and are difficult to scale. The second class of control algorithms are model-based control algorithms. These algorithms use the known model of the system for controller design. Examples of such algorithms include model predictive control (MPC) [7], sliding mode control algorithm [8], linear quadratic regulator (LQR) [9] control, model compensation control (MCC) [10, 11] and active disturbance rejection control (ADRC) [12, 13]. The core of ADRC is the extended state observer (ESO) [14, 15]. ESO belongs to the type I system, and its estimation error is finite. However, it cannot achieve zero error estimation convergence for second-order and higher functions. Nevertheless, ESO still faces problems such as estimation lag, difficult convergence proof and low estimation accuracy. The MCC algorithm [16] involves the compensation function observer (CFO), which can address these issues. The CFO belongs to the type III system and can estimate the constant, slope and acceleration functions without error. MCC effectively improves disturbance suppression by observing external disturbances and the unknown part of the model through the highly accurate CFO. Meanwhile, MCC utilises the known part of the model to improve the tracking effect of each channel [10, 11]. The fields of UAV path planning and obstacle avoidance have widely adopted intelligent technology theory, including neural network [17] and reinforcement learning [18]. These methods are adaptable but also more complex in design.

https://doi.org/10.1017/aer.2024.64 Published online by Cambridge University Press

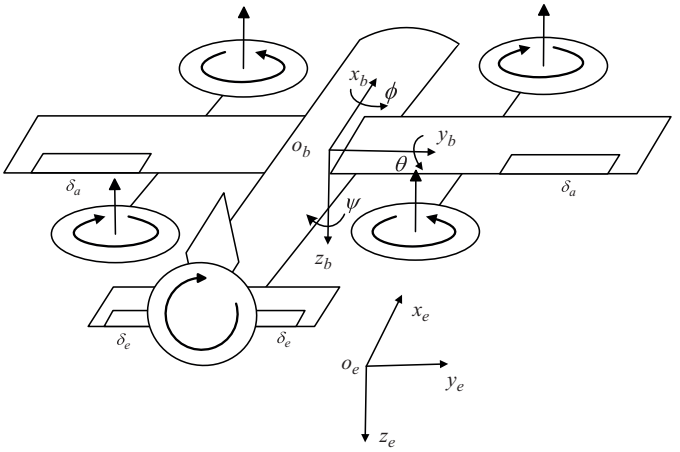

Figure 1. *Configuration of the composite VTOL UAV.*

In summary, the composite VTOL UAV is vulnerable to external disturbances due to the unknown part of its model. Therefore, this paper utilises MCC for the underlying flight control, which can incorporate all model information, including external disturbances and the unknown part of the model.

The paper is structured as follows: Section 2 presents the establishment of the composite VTOL model. Section 3 demonstrates the design of the MCC and its stability analysis. Sections 4 and 5 carry out numerical simulation and hardware-in-loop simulation experiments, comparing the tracking effects of the MCC, ADRC and PID algorithms, and verifying the superiority of the MCC. Section 6 summarises the innovations and contributions made in this paper.

2.0 Composite vertical take-off and landing UAV modeling

The composite VTOL UAV combines both multi-rotor and fixed-wing structures. The multi-rotor propellers, arranged in an 'X' pattern, primarily provide lift for the UAV during multi-rotor flight mode. The fixed-wing propellers, perpendicular to the ground, provide forward thrust for the UAV during fixed-wing flight mode. Figure 1 illustrates the composition of the composite VTOL UAV airframe.

2.1 Multi-rotor section model

The equations for the position and attitude dynamics of the multi-rotor section of the composite VTOL UAV are as follows:

$$\begin{aligned}
\dot{u} &= -\frac{F}{m}(\cos\psi\sin\theta\cos\phi + \sin\psi\sin\phi) + d_{mc_u},\\
\dot{v} &= -\frac{F}{m}(\sin\psi\sin\theta\cos\phi + \cos\psi\sin\phi) + d_{mc_v},\\
\dot{w} &= g - \frac{F}{m}\cos\theta\cos\phi + d_{mc_w},\\
\dot{p} &= \frac{I_y - I_z}{I_x}qr + \frac{1}{I_x}\tau_p + d_{mc_p},\\
\dot{q} &= \frac{I_z - I_x}{I_y}pr + \frac{1}{I_y}\tau_q + d_{mc_q},\\
\dot{r} &= \frac{I_x - I_y}{I_z}pq + \frac{1}{I_z}\tau_r + d_{mc_r}.
\end{aligned} \tag{1}$$

https://doi.org/10.1017/aer.2024.64 Published online by Cambridge University Press

where $u,\ v,\ w$ denote the velocity of the UAV in the body coordinate system, $p,\ q,\ r$ the angular velocity of the UAV in the body coordinate system, $\phi,\ \theta,\ \psi$ the roll angle, pitch angle and yaw angle of the UAV, respectively, m the mass of the UAV, g the gravitational acceleration, F the tensile force exerted on the UAV, $\tau_i\ (i = p,\ q,\ r)$ the torque of the attitude angular channel, $I_i\ (i = x,\ y,\ z)$ the three-axis rotational moment of inertia of the UAV [19], and $d_{mc\_i}\ (i = u,\ v,\ w,\ p,\ q,\ r)$ the total disturbances of the UAV in multi-rotor mode, including model uncertainty and unknown disturbances, such as electromagnetic disturbance, str(ong)winds and rain and other severe weather effects [20]. Additionally, it should be noted that the model is not entirely accurate and relies on small angle assumptions to avoid singularity issues. These assumptions can be considered modeling errors within the system.

2.2 Fixed wing section model

To facilitate the control of the airspeed of the composite VTOL UAV in fixed-wing mode, the dynamics model of the UAV in the airflow coordinate system is introduced [1, 21], i.e.

$$\begin{aligned}\dot{V} = g\ (&-\cos\alpha\cos\beta\sin\theta + \sin\beta\sin\phi\cos\theta + \sin\alpha\cos\beta\cos\theta)\\ &+ \frac{\cos\alpha\cos\beta}{m}T - \frac{D}{m} + d_{fw\_V}.\end{aligned} \tag{2}$$

where V denotes the airspeed of the UAV, $\alpha,\ \beta$ the attack angle and sideslip angle of the UAV, T the thrust applied to the UAV, D the drag applied to the UAV and d_{fw_V} the unknown disturbed part of the UAV in the airspeed channel of the fixed-wing mode, which is mainly the strong wind and the disturbances of the wake [22].

The attitude dynamics model of the UAV is introduced to facilitate the control of the attitude channel of the composite VTOL UAV in fixed-wing mode [1, 21], i.e.

$$\begin{aligned}\dot{p} &= \frac{I_y - I_z}{I_x}qr + \frac{1}{I_x}M_p + d_{fw\_p},\\ \dot{q} &= \frac{I_z - I_x}{I_y}pr + \frac{1}{I_y}M_q + d_{fw\_q},\\ \dot{r} &= \frac{I_x - I_y}{I_z}pq + \frac{1}{I_z}M_r + d_{fw\_r}.\end{aligned} \tag{3}$$

where $d_{fw\_i}\ (i = p,\ q,\ r)$ denotes the unknown part of the UAV in the fixed-wing mode and the external disturbances, $M_i\ (i = p,\ q,\ r)$ the combined moment applied to each channel in the airflow coordinate system, which consists of the following two main parts, i.e.

$$M_i = M_{wi} + M_{Ti},\ \ (i = p,\ q,\ r)\,. \tag{4}$$

where M_{wi} denotes the aerodynamic moment applied to each channel and M_{Ti} the thrust moment applied to each channel. The moment generated by the thrust system is small and can be grouped together into the unknown part of the model when designing the controller due to the small bias angle of the fixed-wing motor. The aerodynamic moment M_{wi} can be expressed as

$$M_{wi} = M_{ia1} + M_{ia2} + M_{ie}. \tag{5}$$

where $M_{ia1},\ M_{ia2},\ M_{ie}$ denote the aerodynamic moments generated by the left aileron, right aileron and elevator. The three-axis aerodynamic moment of each rudder surface $[\,M_{pn}\ \ M_{qn}\ \ M_{rn}\,]^T$ are mainly obtained by the lift and drag forces respectively with the corresponding force arms for the cross-product operation and then accumulate up. The traditional modeling approaches of the composite VTOL UAV obtains the aerodynamic moment of the UAV by multiplying the aerodynamic moment parameters of the three-axis with the dynamic pressure. Cross-product operation is used to model the three-axis aerodynamic moments of the UAV in this paper, which solves the problem of over-reliance on aerodynamic moment parameters in traditional modeling approaches by eliminating the need to identify aerodynamic

https://doi.org/10.1017/aer.2024.64 Published online by Cambridge University Press

moment parameters [23], and makes the model construction more convenient and accurate. Take elevator as an example, i.e.

$$\begin{bmatrix} M_{pe} \\ M_{qe} \\ M_{re} \end{bmatrix} = \begin{bmatrix} M_{peL} \\ M_{qeL} \\ M_{reL} \end{bmatrix} + \begin{bmatrix} M_{peD} \\ M_{qeD} \\ M_{reD} \end{bmatrix} = \begin{bmatrix} x_n \\ y_n \\ z_n \end{bmatrix} \times \begin{bmatrix} 0 \\ 0 \\ -L_e \end{bmatrix} + \begin{bmatrix} x_n \\ y_n \\ z_n \end{bmatrix} \times \begin{bmatrix} -D_e \\ 0 \\ 0 \end{bmatrix}. \tag{6}$$

where M_{ieL} $(i = p,\ q,\ r)$ denotes the three-axis aerodynamic moment generated by the lift force acting on the elevator, M_{ieD} $(i = p,\ q,\ r)$ the three-axis aerodynamic moment generated by the drag force acting on the elevator, x_e, y_e, z_e the position of the elevator force centre with respect to the aircraft's centre of gravity and L_e, D_e the lift force and drag force on the elevator, which are expressed respectively as follows:

$$\begin{aligned} L_e &= C_{le} \cdot Q \cdot S_e, \\ D_e &= C_{de} \cdot Q \cdot S_e. \end{aligned} \tag{7}$$

where Q denotes the dynamic pressure, S_e the area of the elevator, the elevator lift coefficient C_{le} and drag coefficient C_{de} are expressed as follows:

$$\begin{aligned} C_{le} &= cla \cdot \alpha - \delta_e, \\ C_{de} &= |cda \cdot \alpha| \,. \end{aligned} \tag{8}$$

where cla, cda denote the lift and drag parameters and are constants, and δ_e the deflection of the elevator, i.e. the control input. Other rudders and ailerons are the same and do not be repeated here.

Combining Equations (3)–(8) yields model expressions specific to the roll angle and pitch angle channels:

$$\begin{aligned} \dot{p} &= \frac{\left(I_y - I_z\right) qr}{I_x} - \frac{2QS_{a1}y_{a1}}{I_x}\delta_{a1} + d_{fw\_p}, \\ \dot{q} &= \frac{I_z - I_x}{I_y} pr + \frac{QS_e x_e}{I_y}\delta_e - \frac{Q\left(2S_{a1}x_{a1} + S_e x_e\right) cla \cdot \alpha}{I_y} \\ &\quad + \frac{Q\left(2S_{a1}z_{a1} + S_e z_e\right) |cda \cdot \alpha|}{I_y} + d_{fw\_q}. \end{aligned} \tag{9}$$

where δ_{a1}, δ_{a2} denote the deflection of the left aileron and right aileron, x_{a1}, y_{a1}, z_{a1} the position of the force centre of the left aileron relative to the centre of gravity of the UAV. Since the right aileron only y-axis relative position is opposite to the left aileron, the remaining positions are all the same as the left aileron. S_{a1} the area of the left wing. Equation (9) expresses the relevant parameters in terms of the relative parameters of the left aileron for design convenience. Since the UAV design used in this paper does not include a rudder, the yaw channel is not controlled in fixed-wing mode.

3.0 Composite VTOL UAV model compensation controller design and stability analysis

Either channel of a composite VTOL UAV can be written in the form of a second-order system. Here, as an example, the roll channel in fixed-wing mode is used to rewrite the first line of Equation (9) in the following form, i.e.

$$\begin{cases} \dot{\phi} = p, \\ \dot{p} = \dfrac{\left(I_y - I_z\right) qr}{I_x} - \dfrac{2QS_{a1}y_{a1}}{I_x}\delta_{a1} + d_{fw\_p}. \end{cases} \tag{10}$$

where p is the state variable, denoted by x, $\left(I_y - I_z\right) qr/I_x$ is the known part of the model, denoted by f_k, d_{fw_p} is the external disturbances and the unknown part of the model, denoted by f_{uk}, δ_{a1} is the control

https://doi.org/10.1017/aer.2024.64 Published online by Cambridge University Press

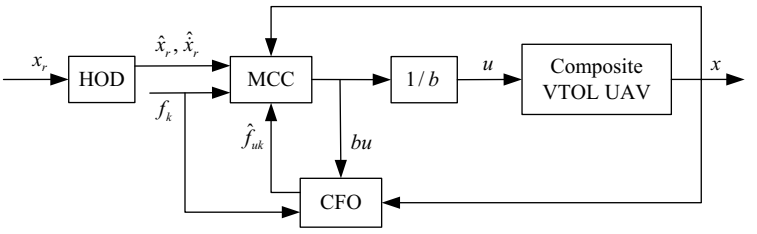

Figure 2. *Block diagram of model compensation controller.*

input, denoted by u, $-2QS_{a1}y_{a1}/I_x$ is the control input coefficient, denoted by b. For the roll angular velocity channel, the general first-order form is as follows:

$$\dot{x} = f_k + f_{uk} + bu. \tag{11}$$

The other angular velocity and velocity channels for the composite VTOL UAV can be expressed as the first-order form of Equation (11).

For the roll angle channel $\dot{\phi} = p$, proportional control can be used:

$$p_r = k_{fw\_\phi}\left(\phi_r - \phi\right). \tag{12}$$

where k_{fw_ϕ} denotes the roll angle control gain in fixed wing mode.

The MCC consists of three main components: the HOD, the CFO and the model compensation control module.

3.1 Model compensation controller

The block diagram of the model compensation controller is shown in Fig. 2.

For the first-order system Equation (11), the second-order model compensation control law is designed as

$$u = \frac{1}{b}\left[k\left(x_r - x\right) + \hat{\dot{x}}_r - f_k - \hat{f}_{uk}\right]. \tag{13}$$

where x_r denotes the tracked target, $\hat{\dot{x}}_r$ denotes the estimation of $\dot{x}_r$ obtained through HOD, the unknown part of the model f_{uk} is obtained through CFO, denoted by $\hat{f}_{uk}$. The fixed-wing roll channel as an example, the expression for the controller of the roll angular velocity can be obtained as follows:

$$\delta_{a1} = -\frac{I_x}{2QS_{a1}y_{a1}}\left[k_{fw\_p}\left(\hat{p}_r - p\right) + \hat{\dot{p}}_r - \frac{\left(I_y - I_z\right)qr}{I_x} - \hat{f}_{uk\_p}\right]. \tag{14}$$

The design of the controllers for the remaining channels of the composite VTOL UAV follows the same approach as the roll channel and will not be reiterated here.

3.2 High order differentiator

To estimate $\dot{x}_r$ in Equation (13), we choose the HOD proposed by Qi et al. [24] in this paper, the dynamic equation of HOD is

$$\begin{aligned}
\dot{x}_{h1} &= x_{h2} + l_1\left(x_r - x_{h1}\right), \\
\dot{x}_{h2} &= x_{h3} + l_2\left(x_r - x_{h1}\right), \\
\dot{x}_{h3} &= l_3\left(x_r - x_{h1}\right).
\end{aligned} \tag{15}$$

https://doi.org/10.1017/aer.2024.64 Published online by Cambridge University Press

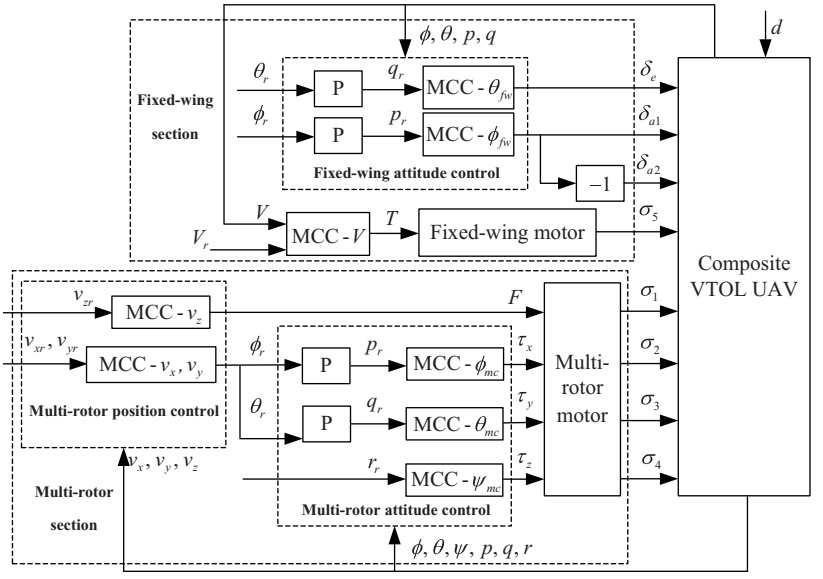

Figure 3. *Overall control block diagram.*

The output equation of HOD is

$$\begin{aligned} \hat{x}_r &= x_{h1}, \\ \hat{\dot{x}}_r &= \dot{x}_{h1} = x_{h2} + l_1 (x_r - x_{h1}) . \end{aligned} \tag{16}$$

where x_r denotes the reference input, x_{hi} $(i = 1, 2, 3)$ the internal state variable of the HOD system, l_i $(i = 1, 2, 3)$ the adjustable parameter, $\hat{\dot{x}}_r$ the estimation of the $\dot{x}_r$. Assuming the HOD system is stabilised, the parameter l_i is uniquely determined by a using the root trajectory method, i.e.

$$l_i = \frac{n^n a}{(n-1)^{n-1}} C_{n-1}^{i-1} a^{i-1} \quad (i = 1, 2, 3) . \tag{17}$$

3.3 Compensation function observer

The second-order CFO [25] proposed by Qi et al. has the specific form

$$\begin{aligned} \dot{z}_1 &= f_k + l e_o + z_2 + bu, \\ \dot{z}_2 &= \lambda l e_o, \\ \hat{f}_{uk} &= l e_o + z_2. \end{aligned} \tag{18}$$

Define $e_c = [\, e_o \quad e_f \,]^T$ as the observation error of the CFO, and e_o, e_f are denoted as

$$e_o = x - z_1, \; e_f = f_{uk} - \hat{f}_{uk}. \tag{19}$$

Its characteristic equation is designed by the method of zero-pole configuration as

$$s^2 + ls + \lambda l = (s + \omega)^2. \tag{20}$$

Yield $l = 2\omega$, $\lambda = 1/2\omega$. Figure 3 shows the overall control block diagram of the composite VTOL UAV.

https://doi.org/10.1017/aer.2024.64 Published online by Cambridge University Press

Table 1. *Main parameters of Eagle UAV*

Symbol	Physic meaning	Value
0.5 px m/kg	quality	7.2
l/m	half-wheelbase	4.12
I_x/kg · m^2	x-axis moment of inertia	4.12
I_y/kg · m^2	y-axis moment of inertia	9.58
I_z/kg · m^2	z-axis moment of inertia	9.85
g/m · s^2	gravitational acceleration	9.8

3.4 Stability analysis of the model compensated controller

Lemma 1. *25: When the Taylor expansion of f_{uk} is second-order infinitesimal, the estimation error of the CFO $e_f = f_{uk} - \hat{f}_{uk}$ can achieve zero steady-state convergence.*

Lemma 2. *10: When x_r is a second-order infinitesimal function and its first-order derivative is constant and bounded, the estimation error of HOD $\tilde{e} = \dot{x}_r - \hat{\dot{x}}_r$ can achieve zero steady-state convergence.*

Theorem 1. *When* Lemmas 1 *and* 2 *hold and $k > 0$, the error of the closed-loop system $e = x_r - x$ based on the model-compensated controller tends to zero.*

The proof of Theorem 1 refers to the literature author10. The idea in the paper is given here as a simple proof procedure.

Proof: define a Lyapunov function

$$V = \tfrac{1}{2}e^2 + \tfrac{1}{2}\tilde{e}^2 + \tfrac{1}{2}e_f^2. \tag{21}$$

Derivation of Equation (20) yields

$$\dot{V} = e\dot{e} + \tilde{e}\dot{\tilde{e}} + e_f\dot{e}_f = e\left(\dot{x}_r - \dot{x}\right) + \tilde{e}\dot{\tilde{e}} + e_f\dot{e}_f. \tag{22}$$

Substituting Equation (13) into the above equation

$$\begin{aligned}\dot{V} &= e\left(\dot{x}_r - f_k - f_{uk} - bu\right) + \tilde{e}\dot{\tilde{e}} + e_f\dot{e}_f \\ &= e\left(\dot{x}_r - \hat{\dot{x}}_r + \hat{f}_{uk} - f_{uk} - k\left(x_r - x\right)\right) + \tilde{e}\dot{\tilde{e}} + e_f\dot{e}_f \\ &= e\left(\tilde{e} - e_f - ke\right) + \tilde{e}\dot{\tilde{e}} + e_f\dot{e}_f \\ &= -ke^2 + \tilde{e}\left(e + \dot{\tilde{e}}\right) + e_f\left(\dot{e}_f - e\right).\end{aligned} \tag{23}$$

According to Lemma 1, the estimation error of HOD tends to zero and the estimation error of CFO tends to zero. Therefore holds.

Proof complete.

4.0 Numerical simulation and analysis

This paper presents a numerical simulation experiment based on an Eagle UAV. Table 1 shows the main parameters of the UAV.

This paper focuses on the following numerical simulation experiments:

- Experiments comparing the estimation performance of two observers, CFO and ESO, with the same parameters, for the same external disturbance are shown in Fig. 4.

https://doi.org/10.1017/aer.2024.64 Published online by Cambridge University Press

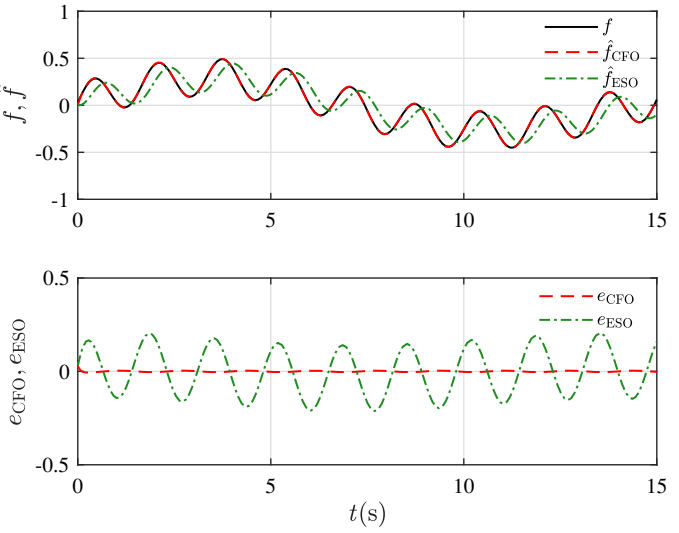

Figure 4. *Comparison of CFO, ESO observer estimation effect.*

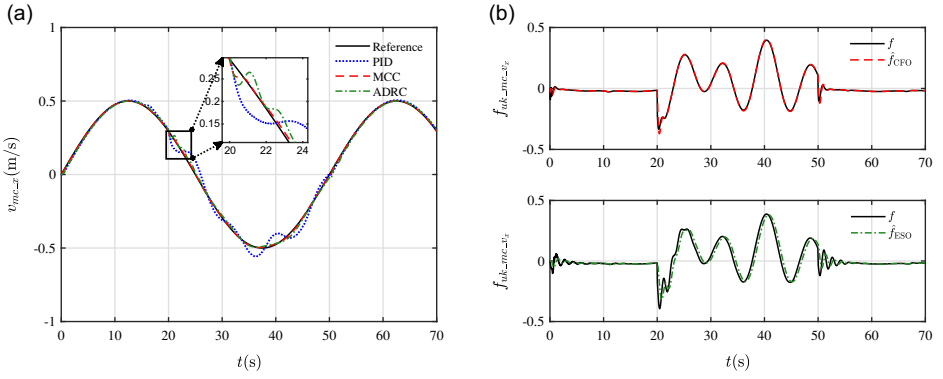

Multi-rotor mode v_x channel effect under disturbances of the composite VTOL UAV.

Comparison of v_x channel observer estimation effect of the composite VTOL UAV.

Figure 5. *Composite VTOL UAV multi-rotor mode simulation effect.*

- The composite VTOL UAV took off in multi-rotor mode and maintained a sinusoidal motion. After 15s, it was kept at a certain altitude, and external disturbance were introduced between 20s and 50s. The experiments plot and analysed the x-axis velocity tracking performance of PID, MCC and ADRC in multi-rotor mode, as well as the estimation performance of CFO and ESO for the perturbation in the x-axis velocity channel in multi-rotor mode. Additionally, the overall flight trajectory of the UAV based on MCC in multi-rotor mode was examined. The results are presented in Figs. 5 and 6.
- The composite VTOL UAV flew at a high altitude with an initial speed of 15m/s in fixed-wing mode and made a spiral upward motion with a speed of 23m/s afterward. An external disturbance was introduced between 20s-50s. The experiments plot and analysed the tracking effects of PID, MCC and ADRC on the roll angle in fixed-wing mode; the estimation effects of CFO and ESO on disturbances in the roll angle loop in the fixed-wing mode; the overall flight trajectory of the UAV based on MCC in fixed-wing mode. The results are presented in Figs. 7 and 8.

https://doi.org/10.1017/aer.2024.64 Published online by Cambridge University Press

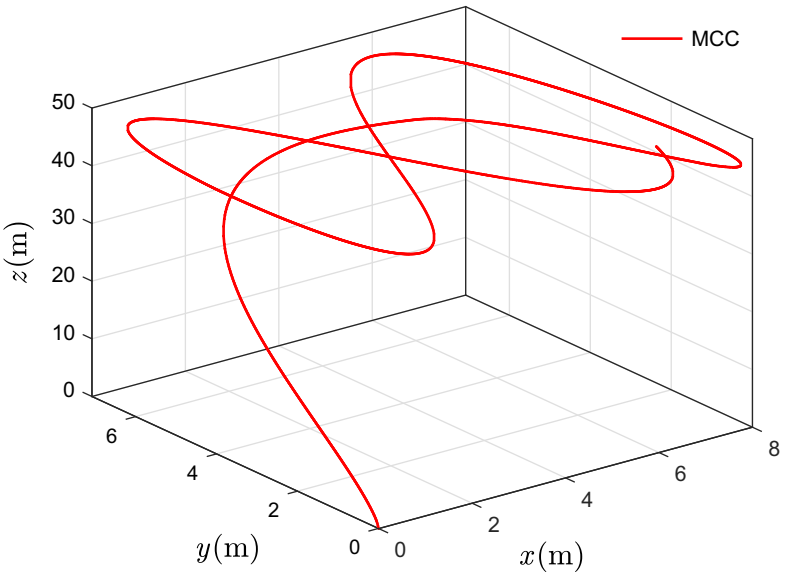

Figure 6. *Overall flight trajectory of the composite VTOL UAV in multi-rotor mode.*

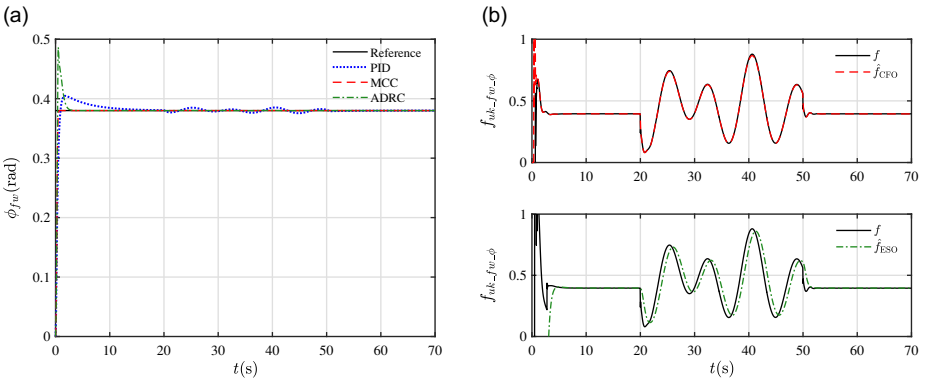

Fixed-wing mode roll channel effect under disturbances of the composite VTOL UAV.

Comparison of roll channel observer estimation effect of the composite VTOL UAV.

Figure 7. *Composite VTOL UAV fixed-wing mode simulation effect.*

- The composite VTOL UAV took off in multi-rotor mode and switched to fixed-wing mode after 15s, then it ascended in a spiral upward motion at 23m/s. The overall MCC-based flight trajectory was finally plotted, as shown in Fig. 9.

This paper is based on the MATLAB/Simulink platform to realise the construction of the control algorithms. Based on this various numerical simulation experiments of composite VTOL UAV can be realised.

4.1 Observer performance analysis

Setting $bu = 1$, the parameters to be rectified of CFO and ESO $\omega = 5$, the nonlinear term is

$$f = 0.2\sin(1.2\pi t) + 0.2\sin(0.4t + 0.1) + 0.1\sin(0.5t + 0.1)\,. \tag{24}$$

https://doi.org/10.1017/aer.2024.64 Published online by Cambridge University Press

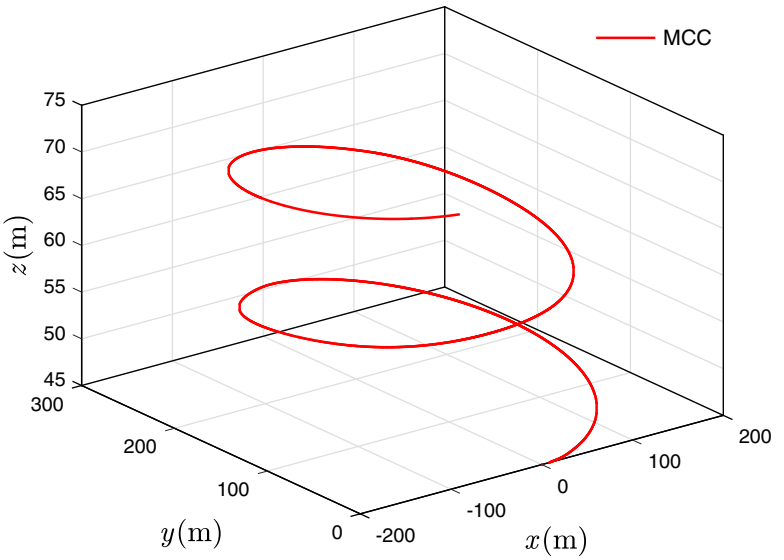

Figure 8. *Overall flight trajectory of the composite VTOL UAV in fixed-wing mode.*

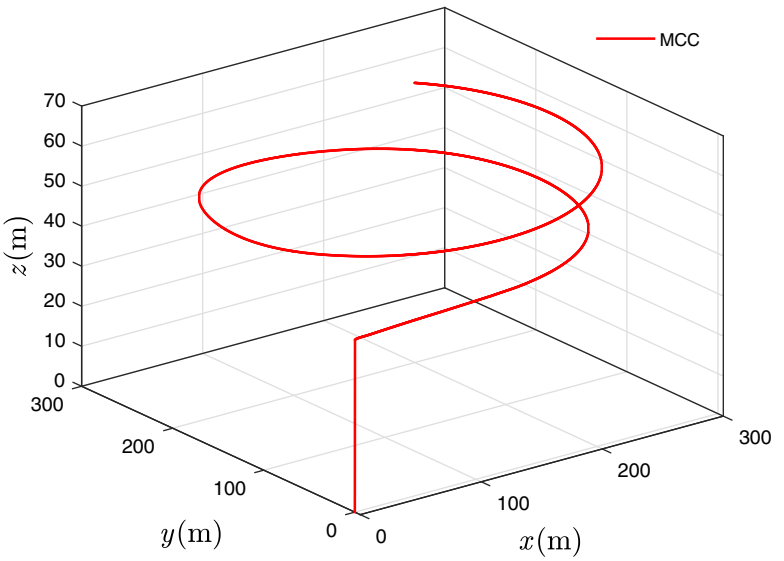

Figure 9. *Overall flight trajectory of the composite VTOL UAV switching from multi-rotor mode to fixed-wing mode.*

Figure 4 shows that the CFO estimation almost coincides with the disturbances, while the ESO estimation curve is obviously lagging and the estimation at the peak is seriously underestimated. The error curves reveal the estimation performance of the two observers. This paper analyses the control performance using the mean absolute error (MAE). The MAE is 0.0031 for CFO and 0.1073 for ESO. The estimation effect of CFO is 97% more effective compared to ESO. Meanwhile, the observation error of ESO is between ± 0.22 and CFO is between ± 0.03, CFO improves by 86% compared to ESO.

https://doi.org/10.1017/aer.2024.64 Published online by Cambridge University Press

Table 2. *Experimental parameters for numerical simulation of multi-rotor mode*

		v_x/v_y	v_z	v_ϕ	v_θ	v_ψ
HOD	h	20	10	10	10	10
TD	r	100	100	100	100	100
	h_0	0.1	0.1	0.1	0.1	0.1
CFO **ESO**	ω	5	3	4	4	3
System parameter	b	1	−0.14	0.24	0.1	0.1
	k_1	10	10	5	5	10
	k_p	3	10	5	5	5
PID	k_i	0.5	3	1	1	0.1
	k_d	1	0.1	0.01	0.01	0.01

4.2 MCC control tracking performance analysis in multi-rotor mode

Sett the initial velocity of the composite VTOL UAV as $[v_{x0},\ v_{y0},\ v_{z0}]$=$[0,\ 0,\ 0]$ (m/s) and the initial attitude angular velocity as $[v_{\phi 0},\ v_{\theta 0},\ v_{\psi 0}] = [0,\ 0,\ 0]$ (rad/s). The velocity of channel x is used as an example to illustrate the tracking and anti-disturbance effects, the desired velocity of each channel are as follows:

$$
\begin{aligned}
v_{xr} &= 0.5\sin\left(0.04\pi t\right)\ (\mathrm{m/s})\ , \\
v_{yr} &= \sin\left(0.09\pi t\right)\ (\mathrm{m/s})\ , \\
v_{zr} &= \begin{cases} -3\ (\mathrm{m/s})\ , (0 < \mathrm{t} < 15), \\ 0\ (\mathrm{m/s})\ , (\mathrm{t} > 15), \end{cases} \\
v_{\psi r} &= 0\ (\mathrm{rad/s})\ .
\end{aligned} \tag{25}
$$

A disturbance is injected into each channel between 20s-50s for the

$$
d = 0.06 + 0.1\sin(0.5t) + 0.02\sin(0.5t + 0.7) + 0.2\sin(0.8t + 0.5)\ . \tag{26}
$$

The simulation time is 70s. Table 2 shows the control parameters of MCC, ADRC and PID, where h denotes the HOD parameter, r, h_0 denote the tracking differentiator (TD) parameters, ω denotes the observer parameter, b denotes the control input parameter, k_1 denotes the controller gain, k_j $(j = p,\ i,\ d)$ denotes the PID control parameter and $k_\phi = k_\theta = 5$ denote the attitude loop P gains.

Figure 5(a) displays the tracking curves for channel v_x. The MCC controller can accurately track the given airspeed. The PID controller exhibits the worst tracking and anti-disturbance capability because it does not utilise feedforward from a known model or feedback from an unknown model. The overshoot of the ADRC is more pronounced due to the lag in the estimation of the disturbances by ESO and the inaccuracy of the peak estimation. During the 30s of external disturbances, the MCC shows only minimal fluctuations due to its excellent anti-disturbance performance. The MAEs are 0.0210 for PID, 0.0021 for MCC and 0.0095 for ADRC, MCC improves 90% compared to PID, 78% compared to ADRC. It is evident that the MCC has a fast-tracking speed and strong anti-disturbance capabilities.

Figure 5(b) displays the estimation effect curves of the two observers. The CFO estimation closely fits the disturbances, while the ESO exhibits a certain lag, since the ESO is a type I system, in contrast to the CFO is a type II system. Therefore, the CFO can more accurately compensate for external disturbances and the unknown part of the model. The MAEs are 0.0030 for CFO and 0.0248 for ESO, CFO improves 88% compared to ESO, CFO improves 88% compared to ESO, indicating that the observer's estimation accuracy significantly impacts control performance.

The final UAV flight trajectory is shown in Figure 6.

https://doi.org/10.1017/aer.2024.64 Published online by Cambridge University Press

Table 3. *Experimental parameters for numerical simulation of fixed-wing mode*

		V	ϕ	θ
HOD	h	5	20	20
TD	r	100	100	100
	h_0	0.1	0.1	0.1
CFO **ESO**	ω	1.5	20	20
System parameter	k_1	10	30	50
PID	k_p	0.5	0.1	2
	k_i	0.02	0.02	0.1
	k_d	0	0.02	0.1

4.3 MCC control tracking performance analysis in fixed-wing mode

Setting the initial position of the composite VTOL UAV as $[x,\ y,\ z] = [0,\ 0,\ 45]$ (m), the initial velocity as $[v_{x0},\ v_{y0},\ v_{z0}] = [15,\ 0,\ 0]$ (m/s), and the initial attitude angular velocity as $[v_{\phi 0},\ v_{\theta 0},\ v_{\psi 0}] = [0,\ 0,\ 0]$ (rad/s). Using the roll channel as an example to illustrate the tracking and anti-disturbance effect, the desired airspeed and attitude angle are as follows:

$$\begin{aligned} \phi_r &= 0.38(\text{rad})\,, \\ \theta_r &= 0.01(\text{rad})\,, \\ V &= 23(\text{m/s})\,. \end{aligned} \tag{27}$$

An external disturbance is injected into each channel between 20s-50s for the

$$d = 0.06 + 0.1\sin(0.5t) + 0.02\sin(0.5t + 0.7) + 0.2\sin(0.8t + 0.5)\,. \tag{28}$$

The simulation time is 70s. Table 3 shows the control parameters of MCC, ADRC and PID, where $k_\phi = 30$ denotes the roll channel P gain and $k_\theta = 50$ denotes the pitch channel P gain.

Figure 7(a) displays the tracking curve of the roll channel. The MCC controller is basically free of overshoot and almost unaffected by disturbances. PID has the worst tracking effect and anti-disturbance capability, which is due to the poor capability to disturbances of the control algorithm that does not depend on the model. ADRC has a large overshoot and has an average estimation of disturbances. For a clearer comparison of tracking performance, we have chosen the data after all of the controllers are stabilised after 5s to make a comparison. The MAEs are 0.0049 for PID, 0.0014 for MCC and 0.0025 for ADRC, MCC improves 71% compared to PID, 44% compared to ADRC. These results indicate that MCC has the best tracking effect and is more robust.

Figure 7(b) displays the estimation curves of the two observers. The estimation of CFO almost coincides with the disturbances and the estimation of ESO has a large lag. This indicates that the CFO estimation outperforms the ESO estimation with the same observer parameters. To facilitate a clearer comparison of the observation performance, we have chosen the data after both observers are stabilised after 5s to make a comparison. The MAEs are 0.0015 for CFO, 0.0389 for ESO, CFO improves 96% compared to ESO, which shows that the lag of the observer is an important factor affecting the observation accuracy of the observer.

The final overall flight trajectory of the UAV under the MCC method is shown in Figure 8.

4.4 Composite vertical takeoff and landing UAV overall flight trajectory

Setting the initial position of the composite VTOL UAV as $[x,\ y,\ z] = [0,\ 0,\ 0]$ (m), the initial speed as $[v_{x0},\ v_{y0},\ v_{z0}\ ] = [\ 0,\ 0,\ 0]$ (m/s). At the beginning of the simulation, the UAV takes off in multi-rotor

https://doi.org/10.1017/aer.2024.64 Published online by Cambridge University Press

mode and climbs upwards with the speed of $v_z = 3(\mathrm{m/s})$, reaches an altitude of 45m in 15s and switches to the fixed-wing mode, and then carries out the spiral climbing movement with the airspeed of 23(m/s). The specific desired commands are shown as follows:

$$t < 15: \begin{cases} v_x = 0(\mathrm{m/s}), \\ v_y = 0(\mathrm{m/s}), \\ v_z = 3(\mathrm{m/s}), \\ v_{\psi r} = 0(\mathrm{rad/s}). \end{cases} \quad t > 15: \begin{cases} V = 23(\mathrm{m/s}), \\ \theta_r = 0.055(\mathrm{rad}), \\ \phi_r = 0.38(\mathrm{rad}), \\ v_{\psi r} = 0(\mathrm{rad/s}). \end{cases} \tag{29}$$

Figure 9 shows the overall flight trajectory of the UAV under the MCC method.

5.0 Hardware-in-loop simulation experiment and analysis

This paper focuses on semi-physical hardware-in-loop simulation experiments. The experiments simulate the scenario of a UAV taking off in multi-rotor mode, switching to fixed-wing mode after 10 seconds, and performing a spiral upward flight.

To simulate disturbances in real flight, this hardware-in-loop experiment uses the Simulink/Uniform Random Number module to randomly generate three types of disturbances. These disturbances are then superimposed and input into the composite VTOL UAV. The upper and lower limits of the three kinds of disturbances are selected as [−1, 1], [−1, 1], [−0.5, 0.5], respectively, and the sampling time is selected as 0.001s. The three kinds of disturbance seeds are selected as 564,565, 6,846,798, 46,545, respectively, the sampling time is selected as 0.001s.

This paper presents simulation experiments that are conducted based on the Rflysim platform. The designed control algorithm is compiled to generate custom C/C++ code through the Pixhawk Support Package (PSP) toolbox in MATLAB/Simulink and downloaded to the real Pixhawk self-pilot system. The hardware-in-loop simulator is formed by the real-time motion simulation software of CopterSim and the 3D visualisation view software of RFlySim3D. The UAV simulation model is configured on CopterSim, which is connected to the Pixhawk autopilot system via USB serial port. The flight data is transmitted in real-time to RflySim3D via UDP to display the UAV's positional status. The Q Ground Control (QGC) is primarily used for initialisation tasks, such as sensor calibration, remote control calibration, and parameter adjustment of the Pixhawk self-pilot before UAV takeoff. The remote-control system comprises a remote controller and a receiver for sending control commands. Based on this hardware-in-loop simulation verification of the algorithm can be achieved. The UAV takes off in multi-rotor mode and climbs upwards with the speed of $v_z = 2$ (m/s), and after 10s switches to the fixed-wing mode, and then carries out the spiral climbing movement with the airspeed of 25(m/s). The specific desired commands are shown as follows:

$$t < 10: \begin{cases} v_x = 0(\mathrm{m/s}), \\ v_y = 0(\mathrm{m/s}), \\ v_z = 2(\mathrm{m/s}), \\ v_{\psi r} = 0(\mathrm{rad/s}). \end{cases} \quad t > 10: \begin{cases} V = 25(\mathrm{m/s}), \\ \theta_r = 0.23(\mathrm{rad}), \\ \phi_r = 0.38(\mathrm{rad}), \\ v_{\psi r} = 0(\mathrm{rad/s}). \end{cases} \tag{30}$$

Figure 10 shows the tracking effect of the roll channel in fixed-wing mode under three control algorithms: PID, MCC and ADRC. MCC can almost track the desired roll angle in the case of the whole access to the disturbances. ADRC exhibits some overshoot when it first receives the command due to the lag in estimating the unknown disturbances by ESO. Meanwhile, ADRC can't respond quickly when it just receives the command. The PID controller is negatively impacted by larger disturbances, the curve is more fluctuating and has the worst anti-disturbance capability. The MAEs are 0.0251 for PID, 0.0111 for MCC, 0.0163 for ADRC, MCC improves 56% compared to PID, 32% compared to ADRC. It is evident that the MCC controller exhibits the best tracking performance in the semi-physical simulation and is the least affected by disturbances.

https://doi.org/10.1017/aer.2024.64 Published online by Cambridge University Press

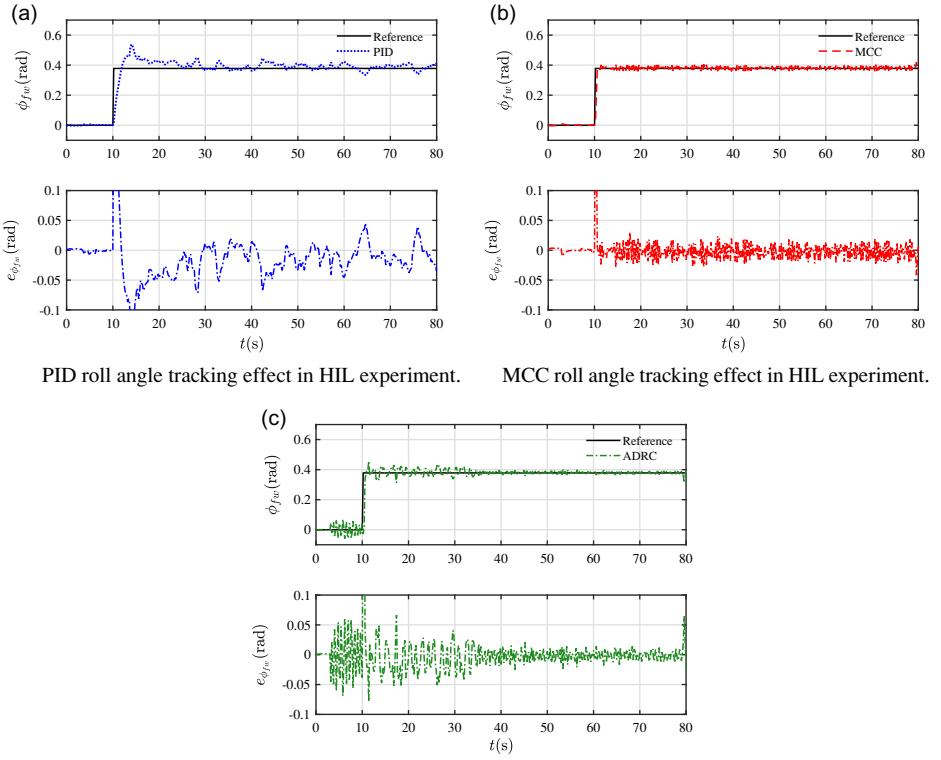

PID roll angle tracking effect in HIL experiment. MCC roll angle tracking effect in HIL experiment.

ADRC roll angle tracking effect in HIL experiment.

Figure 10. *Composite VTOL UAV HIL simulation effect.*

6.0 Conclusion

This paper presents the use of the MCC control algorithm to address the nonlinearity, strong coupling and sensitivity to external disturbances of the composite VTOL UAV system. The stability of the MCC algorithm is also demonstrated. The composite VTOL UAV model is constructed using the modeling approach of calculating the cross product of force and force arm. This approach addresses the issue of relying too heavily on aerodynamic identification parameters in traditional modeling approaches, resulting in increased model accuracy. Numerical and hardware-in-loop simulation experiments are conducted using MATLAB/Simulink and Rflysim simulation platforms. The results indicate that the CFO has a better observation effect than the ESO, and the MCC tracking effect is superior to PID and ADRC. Future work will focus on designing a more reasonable mode switching strategy to prevent unnecessary energy loss when switching between multi-rotor and fixed-wing modes. Additionally, efforts will be made to design a more accurate control algorithm. Outdoor flights will be conducted to verify the effectiveness of the proposed algorithm.

Acknowledgements. This work was supported by the National Natural Science Foundation of China (62303350).

Supplementary material. To view supplementary material for this article, please visit https://doi.org/10.1017/aer.2024.64

References

[1] Wu, S.T. *Flight Control System*, Beihang University Press, 2013.
[2] Ducard, G.J.J. and Allenspach, M. Review of designs and flight control techniques of hybrid and convertible VTOL, *Aerosp. Sci. Technol.*, November 2021, **118**, p. 107035.

[3] Rehan, M., Akram, F., Shahzad, A., Shams, T.A. and Ali, Q. Vertical take-off and landing hybrid unmanned aerial vehicles: An overview, *Aeronaut. J.*, April 2022, **126**, (1306), pp 2017–2057.
[4] Matušů, R. and Prokop, R. Robust stabilization of oblique wing aircraft model using PID controller, *IFAC-PapersOnLine*, 2015, **48**, (14), pp 265–270.
[5] Guo, X.T., Qi, G.Y., Li, X. and Ma, S.L. Chaos control of small-scale UAV helicopter based on high order differential feedback controller, *Int. J. Control*, September 2022, **95**, (9), pp 2473–2484.
[6] Lu, B. Research on the total energy control system of composite VTOL UAV Based on Px4, North China University of Technology, 2020.
[7] Manzoor, T., Xia, Y.Q., Zhai, D.H. and Ma, D. Trajectory tracking control of a VTOL unmanned aerial vehicle using offset-free tracking MPC, *Chin. J. Aeronaut.*, July 2020, **33**, (7), pp 2024–2042.
[8] Mughees, A., Ahmad, I., Mughees, N. and Mughees, A. Conditioned adaptive barrier-based double integral super twisting SMC for trajectory tracking of a quadcopter and hardware in loop using IGWO algorithm, *Expert Syst. Appl.*, January 2024, **235**, p 121141.
[9] Yang, Y.J., Zhu, J.H., Yuan, X.M., Wang, X.Y., Kuang, M.C. and Shi, H. Dynamic characteristics analysis and robust transition control of tail-sitter VTOL UAVs, *Aerosp. Sci. Technol.*, February 2024, **145**, p 108868.
[10] Qi, G.Y., Deng, J.H., Li, X. and Yu, X.C. Compensation function observer-based model-compensation backstepping control and application in anti-inference of quadrotor UAV, *Control Eng. Pract.*, November 2023, **140**, p 105633.
[11] Yao, Q.Q. and Qi, G.Y. Model compensation optimal control for quadrotor UAV system, *Contr Theory Appl.*, 2023.
[12] Yu, B., Kim, S. and Suk, J. Robust control based on ADRC and DOBC for Small-Scale Helicopter, *IFAC-PapersOnLine*, 2019, **52**, (12), pp 140–145.
[13] He, H.X. and Duan, H.B. A multi-strategy pigeon-inspired optimization approach to active disturbance rejection control parameters tuning for vertical take-off and landing fixed-wing UAV, *Chin. J. Aeronaut.*, January 2022, **35**, (1), pp 19–30.
[14] Han, J.Q. From PID to active disturbance rejection control, *IEEE Trans. Ind. Electron.*, 2009, **56**, (3), pp 900–906.
[15] Sun, R.J., Zhou, Z. and Zhu, X.P. Finite-time terminal sliding mode attitude control for tailless full-wing configuration UAVs based on extended state observers and auxiliary compensators, *ISA Trans.*, January 2024, **144**, pp 282–307.
[16] Qi, G.Y., Li, X. and Chen, Z.Q. Problems of extended state observer and proposal of compensation function observer for unknown model and application in UAV, *IEEE Transactions on Systems Man Cybernetics-Systems*, May 2021, **52**, (5), pp 2899–2910.
[17] Niu, Y.B., Yan, X.F., Wang, Y.Z. and Niu, Y.Z. 3D real-time dynamic path planning for UAV based on improved interfered fluid dynamical system and artificial neural network, *Adv. Eng. Inform.*, January 2024, 59, p 102306.
[18] Xia, Y., Shao, X.L., Ding, T.Y. and Liu, J. Prescribed intelligent elliptical pursuing by UAVs: A reinforcement learning policy, *Expert Syst. Appl.*, September 2024, **249**, p 123547.
[19] Quan, Q. *Introduction to Multicopter Design and control*, Springer, 2017.
[20] Li, S.H., Sun, Z.X. and Talpur, M.A. A finite time composite control method for quadrotor UAV with wind disturbance rejection, *Comput. Electr. Eng.*, October 2022, **103**, p 108299.
[21] Beard, R.W. and McLain, T.W. *Small Unmanned Aircraft: Theory and Practice*, Princeton University Press, 2012.
[22] Lu, H., Gao, L., Yan, Y.D., Hou, M.Z. and Wang, C.L. Wind disturbance compensated path-following control for fixed-wing UAVs in arbitrarily strong winds, *Chin. J. Aeronaut.*, February 2024, **37**, (2), pp 431–445.
[23] Durán-Delfín, J.E., García-Beltrán, C.D., Guerrero-Sánchez, M.E., Valencia-Palomo, G. and Hernández-González, O. Modeling and passivity-based control for a convertible fixed-wing VTOL, *Appl. Math. Comput.*, January 2024, **461**, p 128298.
[24] Qi, G.Y., Chen, Z.Q. and Yan, Z.Z. High order differential feedback control for nonlinear systems, *Chaos, Solitons Fractals*, July 2008, **37**, (1), pp 308–315.
[25] Qi, G.Y., Hu, J.B., Li, L.Y. and Li, K. Integral compensation function observer and its application to disturbance-rejection control of QUAV attitude, *IEEE Trans. Cybernet.*, January 2024.

Cite this article: Qi G.Y., Zhang X.R. and Xu L. Model compensation control of composite vertical take-off and landing UAV. *The Aeronautical Journal*, https://doi.org/10.1017/aer.2024.64